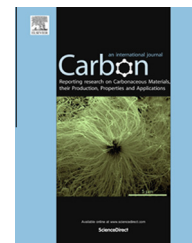


Available at www.sciencedirect.com

ScienceDirect

journal homepage: www.elsevier.com/locate/carbon

High energy density Li-ion capacitor assembled with all graphene-based electrodes



Tengfei Zhang, Fan Zhang, Long Zhang, Yanhong Lu, Yi Zhang, Xi Yang, Yanfeng Ma, Yi Huang*

Key Laboratory of Functional Polymer Materials and Center for Nanoscale Science and Technology, Collaborative Innovation Center of Chemical Science and Engineering, Institute of Polymer Chemistry, College of Chemistry, Nankai University, Tianjin 300071, China

ARTICLE INFO

Article history:

Received 2 February 2015

Accepted 11 March 2015

Available online 17 March 2015

ABSTRACT

To meet the higher requirement of energy storage units, novel devices combining high power performance of supercapacitor and high energy density of Li-ion battery are in urgent demand. Herein we designed and fabricated a Li-ion capacitor device, which is composed of an electrochemical double layer capacitance electrode as the positive electrode and a Li-ion battery type electrode as the negative electrode. Both electrodes consist of graphene-based active materials: a three-dimensional graphene-based porous carbon material with ultrahigh specific surface area, appropriate pore size distribution and excellent conductivity for the positive electrode, and a flash-reduced graphene oxide with open-pore structure and superior rate capability for the negative electrode. With the benefit of the Li-ion capacitor structure, the device exhibits a comprehensive and excellent electrochemical performance in terms of high operating voltage (4.2 V), ultrahigh energy density of 148.3 Wh kg⁻¹ (with power density of 141 W kg⁻¹), maximum power density of 7800 W kg⁻¹ (with energy density kept at 71.5 Wh kg⁻¹) and long cycle life. Such a superior performance indicates that the Li-ion capacitor could be a promising novel energy storage device for wide applications in fast, high efficient and long life energy storage systems.

© 2015 Elsevier Ltd. All rights reserved.

1. Introduction

The rapid development of consumer electronics has changed our lives so profoundly. The future of these electronic products is to become smaller, lighter and smarter, but the slow development of energy storage devices has lagged behind to meet this trend. Besides, environment-friendly electric vehicles and hybrid electric vehicles [1–4], and renewable solar/wind power system with a fluctuation power output all require high performance rechargeable electrical energy storage device with high efficiency, good safety, long cycle life, low cost, short charging time and especially high energy density

without sacrificing power density [3,5,6]. Two of the most important and typical electrochemical energy storage devices, Li-ion batteries (LIBs) and electrochemical capacitors (ECs), also called supercapacitors (SCs) or ultracapacitor [7,8], stand at opposite ends of the spectrum in terms of their power and energy densities [9,10]. Faradaic reactions in the bulk of electrode of LIBs provide high energy density (120–150 Wh kg_{cell}⁻¹), but due to the kinetics-limited charge/discharge, LIBs have low power density (100–1000 W kg_{cell}⁻¹) and long charge/discharge time mostly for hours. Additionally, its cycle life is limited to approximately 1000 cycles [8,11,12]. ECs store energy by either reversible ion adsorption or fast surface redox

* Corresponding author: Fax: +86 2223 499992.

E-mail address: yihuang@nankai.edu.cn (Y. Huang).

<http://dx.doi.org/10.1016/j.carbon.2015.03.032>

0008-6223/© 2015 Elsevier Ltd. All rights reserved.

reactions, of which the former is called electrochemical double layer capacitors (EDLCs) and the latter is called pseudo-capacitors [11]. The mechanism of EDLCs leads to high power density ($10 \text{ kW kg}_{\text{cell}}^{-1}$), long cycle life ($>100,000$) but low energy density ($5\text{--}10 \text{ Wh kg}_{\text{cell}}^{-1}$) [7,8,11,12]. Though fast and reversible redox reactions make pseudo-capacitors achieve higher pseudo-capacitance than EDLCs, poor electrical conductivity and easily damaged structure of the pseudo-capacitance materials lower the power density and cycle stability [13]. Besides, high economic and environmental costs are also the problems that pseudo-capacitors have to face.

It is an obvious pathway to satisfy the fast-growing requirement of energy storage units by improving the power density of LIBs or the energy density of EDLCs dramatically. Since the electrode material is the key factor determining electrical performance of LIBs and EDLCs, lots of efforts have been made to optimize the materials, such as nanostructuring and carbon-coating for LIB materials to improve Li-ion and electron transport rate [3,12,14–16], enlarging the specific surface area (SSA) and controlling/tailoring of pore structure of EDLC materials [8,13,17], and enhancing contact between active electrode materials and current collectors. Meanwhile, novel advanced materials for LIBs [18,19] and EDLCs have also been explored [10,16,20]. Most recently, volumetric energy density and volumetric power density of energy storage devices have been paid attention too because they are important for large scale real-world applications [21], and many approaches focused on novel electrode materials and device configurations have also demonstrated efforts in improving the volumetric performance [22–24].

There is still another promising strategy to bridge LIBs and EDLCs in the Ragone plot. Asymmetric supercapacitors, also called hybrid supercapacitors, combine two different types of electrodes operating on different electrochemical mechanisms—one is an EDLC electrode and the other one contains either a pseudo-capacitance material or a Faradaic material as that used in a battery [4]. Because of the high specific capacity of the pseudo-capacitance material or battery material, and maximum working voltage of the device extended by different potential windows of the two electrodes, such device can obtain significantly improved energy density [25]. If electrode materials for LIBs are chosen to assemble the hybrid supercapacitor, such device is also called Li-ion capacitors (LICs) [8,26–31]. If an EDLC negative electrode (typically activated carbon (AC)) and a LIB positive electrode (such as the spinel structure LiMn_2O_4 or LiCoO_2) are combined, the charge/discharge process is associated with the transfer of the Li-ion between two electrodes [32,33], which is analogue to the “rocking chair” mechanism of LIBs. Owing to the aqueous electrolyte used and the limited specific capacity of positive electrode materials, the operating voltage and energy density of these LICs are restricted. Another more common structure of LIC is the opposite. The LIB anode materials act as the negative electrode and EDLC materials act as the positive electrode, meanwhile non-aqueous electrolytes are chosen. In the charge/discharge process of such structure, the anions in the electrolyte are absorbed/desorbed on the surface of positive electrode materials and simultaneously intercalation/de-intercalation process occurs between Li-ion and LIB negative electrode. Graphite-based materials and

$\text{Li}_4\text{Ti}_5\text{O}_{12}$ (LTO) are mainly two types of commercial LIB anode materials, and AC is most commonly used EDLC material. Consequently, the combination of AC and graphite, or AC and LTO is most typical for LICs [34,35]. Graphite-based materials generally have a higher theoretical specific capacity than LTO (372 mAh g^{-1} for graphite and 175 mAh g^{-1} for LTO), and the high voltage plateau of LTO (about 1.55 V vs Li/Li^+) makes the operating voltage of LIC hardly exceed 3.0 V . Therefore, all carbon-based LIC such as AC-graphite device should achieve highest energy density theoretically.

High power density and good rate performance are also very important for LICs, otherwise it is only transforming a good supercapacitor into a mediocre battery [36]. As the battery type electrode is the main restraining factor for good rate performance of LICs, it is necessary to improve the rate performance of the battery type anode materials. Unfortunately, the Li-ion diffusion coefficient of graphite is very low, novel substituting carbon materials, which have better rate performance but without decreasing specific capacity is an ideal choice. On the other hand, the specific capacitance of commercial AC is still limited, which tends to restrict the energy density of LICs. The full cell energy density of LICs should also be benefited from usage of advanced EDLC materials with higher capacitance. From the discussions above, combination of the EDLC material with optimized specific capacitance and LIB anode material with optimized rate performance will bring comprehensively excellent electrochemical performance of the LIC.

Graphene has captured the imagination of researchers for energy storage. Due to its extraordinary properties such as high theoretical surface area, excellent electrical conductivity, high mechanical strength and potential for low-cost manufacturing, graphene has the potential to develop ideal electrode materials with both high energy density and fast charge/discharge rates [20,37–39]. The key factors to develop advanced graphene-based EC materials, either graphene dominated materials or graphene composite materials (with metallic oxide or conductive polymer), include enlarging the effective SSA, controlling the pore size, avoiding layer stacking and adjusting the dispersion of graphene sheet in the composite material [13,20]. We developed an EDLC material using graphene oxide (GO) and industrial carbon source [17]. This material is a porous three-dimensional (3D) graphene-based bulk material essentially possessing ultrahigh effective SSA, excellent conductivity and desirable pore size distribution, and it has excellent EDLC performance in different electrolytes. It is also well documented that utilizing graphene to promote the high-rate performance of low conductivity LIB materials and accommodate the large volume change of LIB materials such as Si [16,37]. Meanwhile, graphene can also act as the anode material of LIB individually and it has a higher specific capacity than graphite. Using photoflash or laser to reduce GO is a rapid, green and effective method to obtain graphene, and more importantly, it creates an open-pore structure with surface cracks and intersheet voids in the graphene film [9,40,41]. These properties facilitate efficient intercalation kinetics of the Li-ion and make the material be potential as a high-rate capable anode for LIB.

Herein, we employ the above-mentioned porous 3D graphene-based bulk material as the EDLC type positive electrode

and consumer digital camera flash reduced GO (FRGO) as the LIB type negative electrode to assemble all graphene-based LIC. The device has an operating voltage as high as 4.2 V, maximum energy density of $\sim 148.3 \text{ Wh kg}^{-1}$ (with power density of 141 W kg^{-1}) and maximum power density of $\sim 7800 \text{ W kg}^{-1}$ (with energy density of 71.5 Wh kg^{-1}). Moreover, it has an ultra-long cycle life up to 3000 cycles with $\sim 80\%$ capacity retention which is better than most LIBs. Materials with required properties for both electrodes and the synergistic effect realized by LIC structure make this all graphene-based LIC has an excellent and comprehensive performance.

2. Experimental

2.1. Synthesis of porous 3D graphene-based carbon material

The synthesis of porous 3D graphene-based carbon material used for the positive electrode material has been described in our previous work [17]. GO was purchased from Tianjin PlanNano Company. The GO was homogeneously dispersed in water by ultrasonication to form a stable aqueous dispersion (10 mg mL^{-1}). Then phenol (P) and formaldehyde (F) were added to the GO solution, respectively. After stirring for 1 h, the mixture was then transferred to a sealed 100 mL Teflon-lined autoclave, heated up to $180 \text{ }^\circ\text{C}$ and maintained for 12 h. The resulting solid product was then filtered, washed with distilled water and finally dried in vacuum at $120 \text{ }^\circ\text{C}$ for 24 h. This intermediate product was mixed with KOH of 4 times mass of the product and the mixture was then placed in a horizontal tube furnace and heated at $900 \text{ }^\circ\text{C}$ for 1 h at ramp rate of $5 \text{ }^\circ\text{C min}^{-1}$ under Ar gas. After cooling down to the room temperature, the product was thoroughly washed with 0.1 M HCl to remove inorganic salts, then washed with distilled water until the pH value reached 7 and finally dried in vacuum at $120 \text{ }^\circ\text{C}$ for 24 h. The optimized weight feed ratio of (P + F)/GO was 16 and this final product was called PF16 for short. It acted as the EDLC electrode material for the LIC studies.

2.2. Synthesis of FRGO

The negative electrode material FRGO was synthesized by the following procedure. GO was homogeneously dispersed in water by ultrasonication to form a stable aqueous dispersion (2 mg mL^{-1}). Then GO film was obtained by vacuum filtration of GO solution using microporous membrane (50 mm in diameter, $0.22 \text{ }\mu\text{m}$ pore size, Ameritech). The thickness of the GO film was about $15\text{--}20 \text{ }\mu\text{m}$, which could be adjusted through varying the amount of GO solution. The obtained GO film was punched into discs with required diameters of 8, 10, 12 and 14 mm, respectively. Then the small disc was shined with simple digital camera photoflash (Canon EOS 550D or TRIPOD JD730C) at a distance of $\sim 1 \text{ cm}$ for several times until the weight of the disc no longer decreased, and a uniform FRGO disc was obtained.

2.3. Characterization

Scanning Electron Microscopy (SEM) images were obtained on a FEI NanoSem 430 field emission scanning electron

microscope using an accelerating voltage of 5 kV or 10 kV, and Energy Dispersive X-ray Spectroscopy (EDS) was obtained by the AMETEK EDAX detect module on the microscope. Atomic Force Microscopy (AFM) was conducted on a Multimode SPM (Digital Instruments) with a Bruker Nanoscope IIIa Controller. Transmission electron microscopy (TEM) was carried out on a JEOL TEM-2100 transmission electron microscope operated at 200 kV. Raman spectra were performed on a Renishaw inVia Raman spectrometer using laser excitation at 514.5 nm. X-ray Photoelectron Spectroscopy (XPS) was carried out using an AXIS HIS 165 spectrometer (Kratos Analytical) with a monochromatized Al $K\alpha$ X-ray source (1486.7 eV) to analyze the chemical composition of the materials. Elemental analysis (EA) was carried out at Vario Micro cube (Elementar, Germany) for determination of the C, H, and O content. Thermogravimetric analysis (TGA) was done by a Thermogravimetric analyzer (Mettler Toledo, TGA/DSC1) at ramp rate of $10 \text{ }^\circ\text{C min}^{-1}$ under N_2 atmosphere. X-ray Diffraction (XRD) measurements were carried out on a Rigaku D/Max-2500 diffractometer using Cu $K\alpha$ radiation. Nitrogen adsorption-desorption analysis was conducted at 77 K on a Micromeritics ASAP 2020 apparatus. The surface area was calculated by the BET method based on adsorption data in the relative pressure (P/P_0) range of 0.05–0.3. The pore size distribution was analyzed using a NL-DFT method with a slit pore model from the nitrogen adsorption data.

2.4. Fabrication of symmetric supercapacitor, half-cell and LIC

All the symmetric supercapacitor structure devices were fabricated using the industry standard method, and evaluated using the two-electrode industry level device following the method recommended best for industry practice [42,43] to get reliable performance data. For fabricating of EDLC type electrode (as positive electrode of LIC), PF16 powder was mixed directly with 10% polytetrafluoroethylene (PTFE, Dupont), and rolled into thin sheets, which were then punched into 1 cm diameter electrodes and hot pressed onto aluminum foil with conducting carbon coating. The effective loading density of PF16 electrode was typically at $\sim 3.0 \text{ mg cm}^{-2}$ and the loading density could be adjusted by varying the thickness of PF16/PTFE mixture thin sheet. Commercial AC RP20, as contrasting EDLC material, was mixed with super P and PTFE (85:5:10), then followed by the same procedure to fabricate electrode. The loading density of RP20 electrode was typically at $\sim 9.0 \text{ mg cm}^{-2}$ with the similar thickness of PF16 electrode. For fabrication of battery type electrode, an FRGO disc was put on a small disc of Cu foil with a slightly larger diameter, and then pressed and rolled repeatedly with a stainless steel rod. The FRGO disc which obtained from the GO film with a thickness of $15\text{--}20 \text{ }\mu\text{m}$ was reduced most effectively under photoflash exposure [41] and exhibited the best electrochemical performance (among FRGO discs from GO film with different thickness), then the effective mass of FRGO electrode could be adjusted slightly by changing the diameter of FRGO disc. The FRGO electrode disc with a diameter of 1 cm was $\sim 0.8 \text{ mg}$ (about 1 mg cm^{-2}). The symmetric supercapacitor device was assembled with two identical PF16 electrode and denoted as PF16//PF16. Similarly, the

symmetric supercapacitor RP20//RP20 had the same structure except using PR20 electrode. Both EDLC type electrode (PF16 or RP20) and battery type electrode (FRGO) were assembled with lithium metal foil which acted as the counter and reference electrode both to fabricate half-cells (coin-type cell structure). The half-cells were assembled for measuring the performance of each electrode material separately and denoted as PF16//Li, RP20//Li and FRGO//Li, respectively. LIC devices were assembled in coin cells with PF16 electrode and FRGO electrode, denoted as PF16//FRGO. The FRGO electrode was pre-activated through charging and discharging for several cycles at low current density. For mass matching of two different electrodes of LIC, PF16 electrode with required mass could be obtained by adjusting the thickness of electrode disc while the diameter and mass of the FRGO electrode disc was fixed. All the devices above mentioned employed 1 M LiPF₆ dissolved in 1:1:1 (v/v/v) mixture of ethylene carbonate/diethyl carbonate/dimethyl carbonate (EC/DEC/DMC) as the electrolyte. The amount of electrolyte in one coin cell was about 0.4–0.5 mL. The separators in all devices are all Celgard monolayer polypropylene separator 2400.

2.5. Electrochemical measurements

All the electrochemical tests on different types of devices were carried out at room temperature. Cyclic voltammetry (CV) studies were performed at different scan rates and electrochemical potential windows with a LK98B II microcomputer-based electrochemical analyzer (LANLIKE). Electrical impedance spectroscopy (EIS) studies were performed using Autolab (Metrohm), and the measurement frequency ranges were as follows: PF16//PF16, 0.1 MHz–10 mHz; PF16//Li, 1 MHz–10 mHz; FRGO//Li, 1 MHz–1 mHz; PF16//FRGO, 1 MHz–10 mHz. Galvanostatic charge–discharge measurements of symmetric supercapacitors, half-cells, and LICs were carried out galvanostatically at various current densities with voltage windows specific to the materials using battery test systems (LAND CT2001A model, Wuhan LAND Electronics. Ltd and Multi-Stations, Multi-Electrodes PST/GST, Arbin).

The specific capacitance C_s (F g⁻¹) of PF16 (or RP20) in the symmetric supercapacitor was calculated according to the following formula:

$$C_s = 4I/(m dV/dt) \quad (1)$$

where I (A) is the constant current, m (g) is the total active materials mass of two electrodes, and dV/dt (V s⁻¹) is the slope obtained by fitting a straight line to the discharge curve of the symmetric supercapacitor.

The energy density values E (Wh kg⁻¹) of symmetric supercapacitors and LICs were obtained by mathematical integration of the V - Q curve (or V - t curve, as the current density I is a constant value) of the discharge process, using the formula (followed by unit conversion to Wh kg⁻¹):

$$E = \int_{Q_1}^{Q_2} V dQ = \int_{t_1}^{t_2} IV dt \quad (2)$$

where V (V) is the voltage, Q (mAh g⁻¹ or Ah kg⁻¹) is specific discharge capacity, I (A g⁻¹) is the current density, and t (s) is the time of the discharge process. The average power

density values P (W kg⁻¹) of symmetric supercapacitors and LICs were calculated according to the following formula:

$$P = E/\Delta t \quad (3)$$

where Δt is the discharge time.

3. Results and discussion

For better comparison of our materials and device performance with that of conventional ones, in this section, the electrochemical performance of positive electrode material PF16 will be firstly discussed, then followed by the negative electrode material FRGO. At last, the LIC which is assembled with PF16 and FRGO will be investigated.

3.1. Electrochemical performance of PF16 in LiPF₆ electrolyte

Before an LIC device was assembled, the properties and electrochemical performances of all electrode materials have to be studied and understood entirely. As mentioned in the synthesis section and our related work [17], PF16 was obtained by using GO and industrial carbon source. This 3D graphene-based bulk material, with a highly porous structure composed of extremely curved single-layered graphene sheets in the size of a few nanometers, has a ultrahigh BET SSA of 3523 m² g⁻¹ and well-controlled pore size (mostly ranged from 1 to 7 nm and provided better accessibility and more effective SSA for electrolyte ions). Besides, the bulk material also shows excellent conductivity of ~303 S m⁻¹ [17]. All these properties of PF16 should result in an excellent EDLC performance.

To examine the EDLC performance of PF16 in the LiPF₆ electrolyte, there are two kinds of device structures—symmetric supercapacitor containing two identical PF16 electrodes and half-cell device containing PF16 electrode and Li metal foil, both of which utilize LiPF₆-based organic electrolyte. Fig. 1a shows the CV curves of the supercapacitor device PF16//PF16, where the almost rectangular voltammetry characteristics under different scan rates could be observed, indicating a nearly ideal EDLC performance. Galvanostatic charge–discharge curves of PF16//PF16 under different current densities (Fig. 1b) are all nearly straight lines, which also illustrates a standard capacitive behavior of EDLC type supercapacitor with a good rate performance. The specific capacitance of PF16 in Li-ion electrolyte is more than 160 F g⁻¹ at 0.1 A g⁻¹ and about 130 F g⁻¹ at 5 A g⁻¹ and the energy density of PF16//PF16 reached to 41–27.7 Wh kg⁻¹ at the same ranged current densities (Fig. 1c).

The electrochemical performance of PF16 was also studied by fabricating half-cell PF16//Li. The CV (Fig. 1d) and galvanostatic charge–discharge results (Fig. 1e) show that the PF16 has a nearly perfect and fast anions absorption/desorption behavior in the potential range of 2.0–4.0 V vs Li/Li⁺. The specific capacity of PF16 obtained from this device at current densities ranging from 0.1 to 5 A g⁻¹ is plotted in Fig. 1f. As the discharge curve are almost straight lines, specific capacitance of PF16 could be obtained by simply dividing specific capacity by corresponding discharge voltage range (2 V), and the result is also plotted in Fig. 1f. Furthermore, as shown

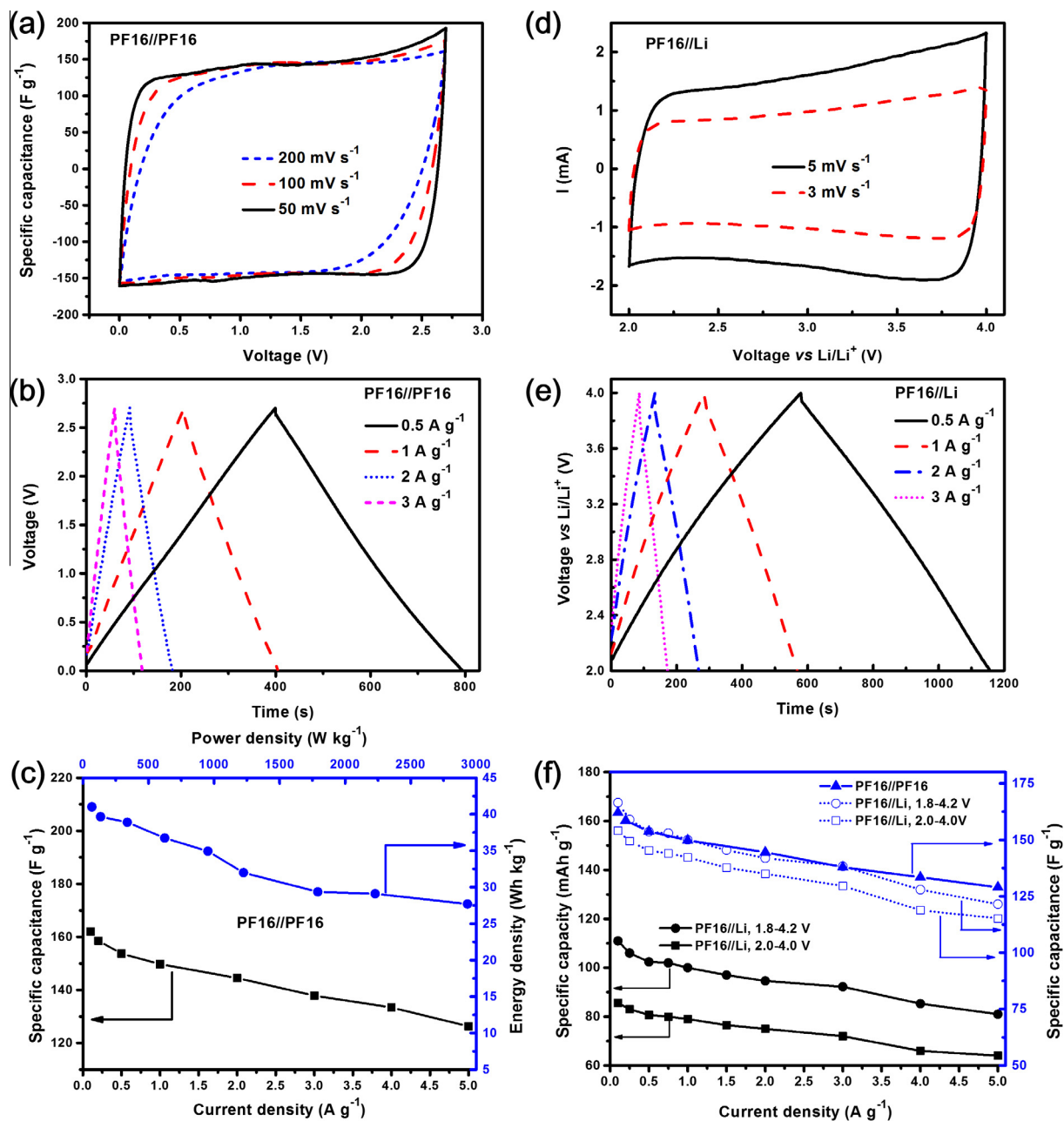


Fig. 1 – Electrochemical performance of PF16 in LiPF_6 electrolyte. (a) CV curves of supercapacitor PF16//PF16 in various scan rates of 200, 100 and 50 mV s^{-1} . (b) Galvanostatic charge–discharge curves of supercapacitor PF16//PF16 at different current densities of 0.5, 1, 2 and 3 A g^{-1} . (c) Specific capacitance of PF16 in supercapacitor PF16//PF16 device at different current densities, and corresponding energy and power densities of PF16//PF16 device. (d) CV curves of half-cell device PF16//Li at different scan rates of 5 and 3 mV s^{-1} , and the electrochemical window was 2.0–4.0 V vs Li/Li^+ . (e) Galvanostatic charge–discharge curves of half-cell device PF16//Li at different current densities of 0.5, 1, 2 and 3 A g^{-1} , and the voltage window was also 2.0–4.0 V vs Li/Li^+ . (f) Specific capacity of PF16 obtained from supercapacitor PF16//PF16 at different current densities. Specific capacity and corresponding specific capacitance of PF16 obtained from half-cell device PF16//Li at different current densities and electrochemical windows. (A color version of this figure can be viewed online.)

in Figs. S1 and S2, in a broader electrochemical potential window of 1.8–4.2 V vs Li/Li^+ , the PF16 still performed as an EDLC type material and had no obvious redox reaction. The specific capacity and specific capacitance of PF16 in 1.8–4.2 V vs Li/Li^+ under different current densities obtained from PF16//Li device are also shown in Fig. 1f. We found that as an EDLC material, PF16 exhibits nonuniform specific capacitance

distribution in different electrochemical potential ranges, which is slightly larger in a higher potential range (vs Li/Li^+), as shown in Figs. 1d,f and S1. Note, the specific capacitance of PF16 in the potential range of 1.8–4.2 V vs Li/Li^+ , calculated from the experimental specific capacity result of the half-cell PF16//Li, matched very well with the experimental specific capacitance result from the symmetric supercapacitor

PF16//PF16 in a broad current density range (Fig. 1f), and this indicates the electrochemical performance data of PF16 in Li-ion electrolyte using both methods are reliable. Besides, the specific capacity retention of PF16 was still 89% of the initial value after even 7000 charge/discharge cycles in the 2.0–4.0 V vs Li/Li⁺ (Fig. S3). In contrast, the common commercial AC–PR20 has only a specific capacitance of $\sim 113 \text{ F g}^{-1}$ even at a small current density (0.25 A g^{-1}) and decreases to 102 F g^{-1} just at 1.5 A g^{-1} (Fig. S4). Such specific capacitance as well as the rate performance is far worse compared with PF16. Based on its excellent EDLC performance in LiPF₆ electrolyte and appropriate electrochemical potential window, PF16 is expected to be an EDLC electrode material for LIC with preminent electrochemical performance.

3.2. Characterization and electrochemical performance of FRGO in LiPF₆ electrolyte

As described in the synthesis section, a free-standing GO film can be reduced by multiple exposure of a focused digital camera photoflash. Such a reduction or deoxygenation process

accompanied with a clear “Po” sound, and the smooth and lustrous surface of GO film turned to be rough, black and lack-luster (Fig. 2a). From the side view optical image of a partially flash reduced GO film (Fig. 2b), the thickness of the flash reduced part of the film (left side part) expanded distinctly compared with the unreduced GO film (right part of the film). The photoacoustic effect, morphology change and thickness increase demonstrate the photothermal reduced mechanism [40]. Because of the efficient light absorption and photothermal conversion of the GO film, combined with the fast energy output of flash in a very short time, the temperature of the GO film would increase and this initiated an instantaneous thermal heating-induced deoxygenation [44,45]. And the pressure between the GO sheets which was generated by the rapid degassing caused the photoacoustic phenomenon and the changes of morphology and thickness [40,41]. Furthermore, the reduction of surface layer of GO film into FRGO could improve the photo absorption and photothermal conversion efficiency, and triggered better flash reduction effect with the following multiple flash exposure. Top view SEM images of GO film (Fig. 2c) and FRGO film (Figs. 2d and e) show that

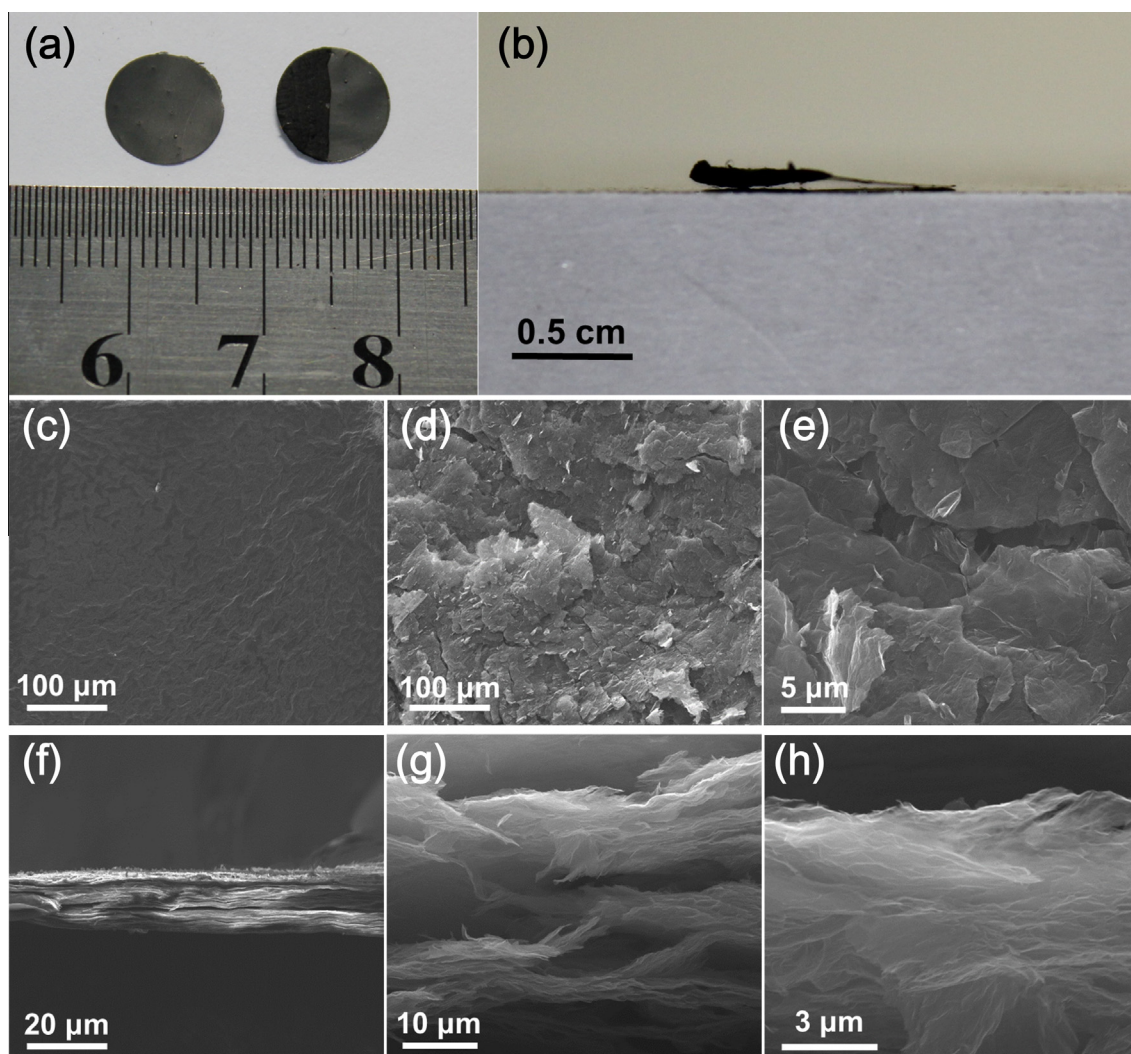


Fig. 2 – Optical images of top view of GO film disc and partially reduced GO film disc (a), and side view of partially reduced GO film disc (b). (c) and (f) are the top view and side view SEM images of GO film, respectively. (d) and (e) are the top view SEM images of FRGO film, (g) and (h) are the side view images of FRGO film. (A color version of this figure can be viewed online.)

rapid degassing in the flash reduction process up-warps the graphene sheets and creates micro pores and cracks clearly. This should also make the underlying graphene sheets to be exposed and reduced efficiently. The side view SEM image of GO film (Fig. 2f) demonstrates that the GO sheets are tightly stacked, and the cross-sectional SEM images of FRGO film (Figs. 2g and h) show that a quite expanded structure and large voids and pathways between the highly warped graphene sheets are formed. A high BET SSA ($277 \text{ m}^2 \text{ g}^{-1}$) of FRGO (Fig. S5) also indicates its loose and open-pore structure (the pore size is mainly larger than 5 nm), which should enable the Li-ion shuttling through the graphene sheets rapidly and efficiently, thus enhanced the lithium intercalation kinetics at ultrafast charge/discharge rates.

The TGA of GO and FRGO films are shown in Fig. S6, the disappearance of distinct mass loss near the temperature of 200°C of FRGO compared with GO indicates that flash reduction is efficient, and FRGO has a quite low oxygen content as well as high carbon content ($\sim 95\%$), which is consistent with the EDS result (carbon content at $\sim 93.4\%$). The deoxygenation effect of flash reduction is also certified by the C/O mass ratio which increased from 1.4 of GO to 6.1 of FRGO based on the EA results. The XPS results shown in Fig. S7 also demonstrate noteworthy deoxygenation of FRGO compared with GO, and the higher C content (98.2%) given by XPS should be due to

the surface effect of XPS measurement. Raman spectrum of FRGO exhibits an increase of I_G/I_D and indicates the recovery of π electronic conjugation (Fig. S8). All these evidences of high C content and recovered sp^2 structure of FRGO are also consistent with its enhanced conductivity compared with GO ($\sim 1.1 \times 10^{-3} \text{ S m}^{-1}$ of GO film [41,45] and $\sim 320 \text{ S m}^{-1}$ of FRGO film). This should improve the rate performance of FRGO as well. Though the TEM (Fig. S9) and AFM (Fig. S10) of FRGO show it is mostly composed of 3–5 layers of graphene sheets, but the interlayer spacing (0.392 nm) is significantly larger than graphite (0.335 nm) (Fig. S11). And for the whole FRGO film, overall the long-range restacking of graphene sheets is very weak indicated by XRD (Fig. S11). Even though the FRGO film should be pressed when used as electrode, no serious graphene sheet restacking occurred in such a process (Fig. S11). These ensure the channels for Li-ion fast passing in and out.

The electrochemical performance of FRGO was investigated using a half-cell device FRGO//Li. Fig. 3a shows the CV curves of FRGO in the potential window of 0–3 V vs Li/Li⁺. There are no obvious peaks in a wide voltage scan rate range from 10 to 0.2 mV s^{-1} which is very different from graphite, whose lithium storage mainly happens in the low potential vs Li/Li⁺. Such a property is also reflected in the charge–discharge curves shown in Fig. 3b, where the voltage

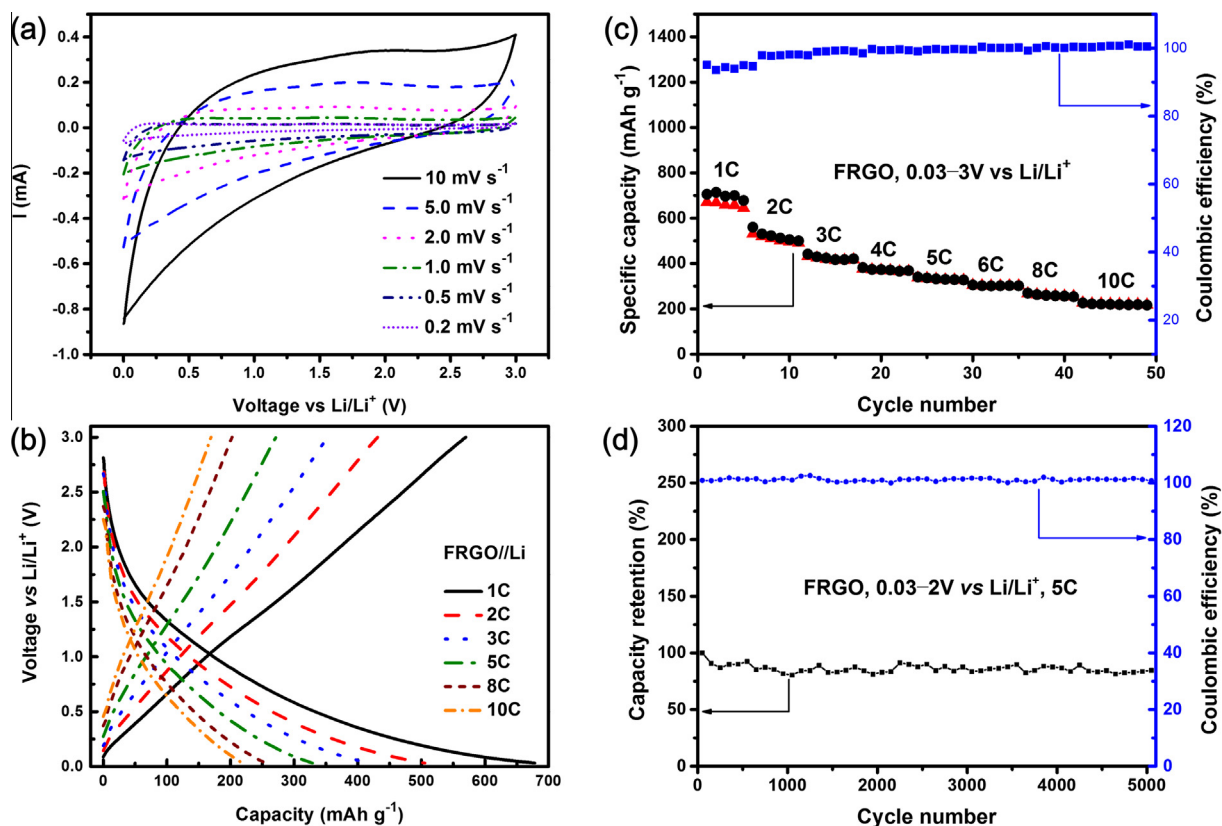


Fig. 3 – (a) CV curves of FRGO at different scan rates in the potential range of 0–3 V vs Li/Li⁺. (b) Charge–discharge curves of FRGO at different current densities of 1–10 C (1 C = 372 mA g^{-1}). (c) Rate performance and corresponding Coulombic efficiency of FRGO at different current densities in the potential range of 0.03–3 V vs Li/Li⁺. (d) Cycle stability of FRGO in the 0.03–2 V vs Li/Li⁺ at a current density of 1.86 A g^{-1} (5 C) for more than 5000 cycles, with high Coulombic efficiency of nearly 100%. (A color version of this figure can be viewed online.)

profiles from 1 C to 10 C (1 C = 372 mA g⁻¹) have no potential plateau in charge/discharge process. Because of the high SSA of FRGO, the initial Coulombic efficiency is around 65–75%, which is primarily caused by the formation of solid electrolyte interface (SEI) film. But after 2–3 charge/discharge cycles at 2 C, a reversible specific capacity of more than 660 mAh g⁻¹ at 1 C with a Coulombic efficiency >95% is obtained, and the specific capacity retains still at ~220 mAh g⁻¹ under a high rate of 10 C (3.72 A g⁻¹) with an almost 100% Coulombic efficiency (Fig. 3c). The high specific capacity and excellent rate performance are attributed to the special lithium storage mechanism of graphene [16,20,46–48] (such as intercalation of Li-ion into both sides of graphene sheets [49,50], micropore lithium storage mechanism [51]), as well as high SSA, good conductivity and open-pore structure of FRGO.

Because PF16 performed excellent EDLC property in the potential window of 2–4 V vs Li/Li⁺, for the potential window matching we could utilize the capacity of FRGO in the potential range of 0–2 V vs Li/Li⁺. Though we could get the electrochemical data from the result of FRGO//Li device operated in 0.03–3 V vs Li/Li⁺ directly, a more credible method is from the charge/discharge measurement of the FRGO//Li half-cell in 0.03–2 V vs Li/Li⁺. The CV curves (Fig. S12), voltage profiles of charge–discharge (Fig. S13) and rate performance (Fig. S14) of such a device show the same good electrochemical performance in a smaller potential window. More importantly, the cycle stability of FRGO in LiPF₆ electrolyte is excellent. The specific capacity still kept ~85% retention even after 5000 charge/discharge cycles at a high current density of 1.86 A g⁻¹ (Fig. 3d). Such an extraordinary electrochemical performance of FRGO make it a good candidate for assembling LIC with improved energy density and power density.

3.3. Performance of LIC assembled with PF16 and FRGO

As discussed above, PF16 and FRGO both have excellent electrochemical performances and should be the promising EDLC type and battery type electrode materials for high-energy LIC. In order to further investigate the potential superiority, we designed and assembled an LIC, which contained PF16 as the positive electrode, FRGO as the negative electrode and LiPF₆-containing organic electrolyte. In the charge process of this LIC, PF₆⁻ are absorbed in the micropores of PF16 and the potential of this EDLC electrode increases, while the Li⁺ from the electrolyte are intercalated/stored in FRGO and the potential of this battery electrode decreases, thus the voltage of LIC increases and electric energy can be stored. The discharge process is completely reversible (Fig. 4).

Different from the symmetric supercapacitor, the LIC has two kinds of electrode materials in positive and negative electrodes, respectively, and these two electrode materials work in different electrochemical potential windows and exhibit different specific capacities. To obtain high energy density of LIC, working potential ranges of both electrodes have to be matched for maximizing those potencies. Based on above investigation of PF16 and FRGO, we consider distributing the potential range of 2–4 V vs Li/Li⁺ to PF16 electrode and 0.03–2 V vs Li/Li⁺ to FRGO electrode, respectively and the maximum voltage of the LIC could reach up to 4 V. According to the equation of $Q_+ = Q_- = m_+q_+ = m_-q_-$ (where Q and q are the

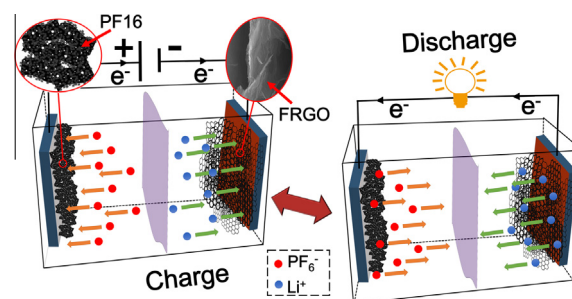


Fig. 4 – Schematic of the charge/discharge mechanism of our LIC based on PF16 and FRGO. (A color version of this figure can be viewed online.)

capacity and specific capacity, m is the mass of active electrode material, and subscripts stand for the positive and negative electrode), the respective masses of the two electrodes must be adjusted to equalize the total capacity. The specific capacities of PF16 and FRGO in their designed working potential windows are about 90–80 mAh g⁻¹ at the current densities of 0.1–0.5 A g⁻¹ and 350–280 mAh g⁻¹ at the current densities of 0.372–0.744 A g⁻¹, respectively. So theoretically, the best mass ratio of two electrodes (m_+/m_-) should be at 3.5–4.0, considering the different rate performances of PF16 and FRGO [27,52,53].

PF16//FRGO devices with different mass ratios were charged/discharged in the voltage range of 0–4 V to investigate their electrochemical performance. The CV curve of LIC ($m_+/m_- = 3.5$) is shown in Fig. 5a, which shows a larger integration area in the high voltage range that is different from rectangular shape curve of symmetric supercapacitor. This means that the LIC can store more energy than symmetric supercapacitor owing to the synergistic effect of two different energy-storage mechanisms in LIC. CV curves of LIC ($m_+/m_- = 4.0$) at different voltage scan rates show the similar results (Fig. S15). Fig. 5b displays the galvanostatic charge–discharge curves of LIC ($m_+/m_- = 3.5$) at different current densities (based on the negative electrode). The curves are quite similar with the supercapacitor type device, because the FRGO has an approximate linear voltage profiles and no potential plateau. The Ragone plots of LICs with mass ratios from 2.0 to 7.0 and supercapacitor PF16//PF16 as contrast are shown in Figs. 5c and d for exhibiting their comprehensive performance. The LIC with a mass ratio of 3.5 shows a maximum energy density of 128 Wh kg⁻¹ based on the total active material mass of both electrodes. This energy density is more than three times higher than that of symmetric supercapacitor PF16//PF16. Fig. 5d also shows that LIC with a mass ratio of 4.0 has a better performance when the current density is high (high power density region in the Ragone plots), and the energy density still achieves 71.5 Wh kg⁻¹ while the power density is as high as 7800 W kg⁻¹. Such a change of the best mass ratio at different current densities could be caused by the following reasons. Firstly, the rate performances of PF16 and FRGO are different and the specific capacity of FRGO decreases more quickly than the PF16 with the increase of current density, so the best mass ratio at different current density should be different theoretically. Secondly, because the electrochemical behaviors of the two electrodes of LIC are

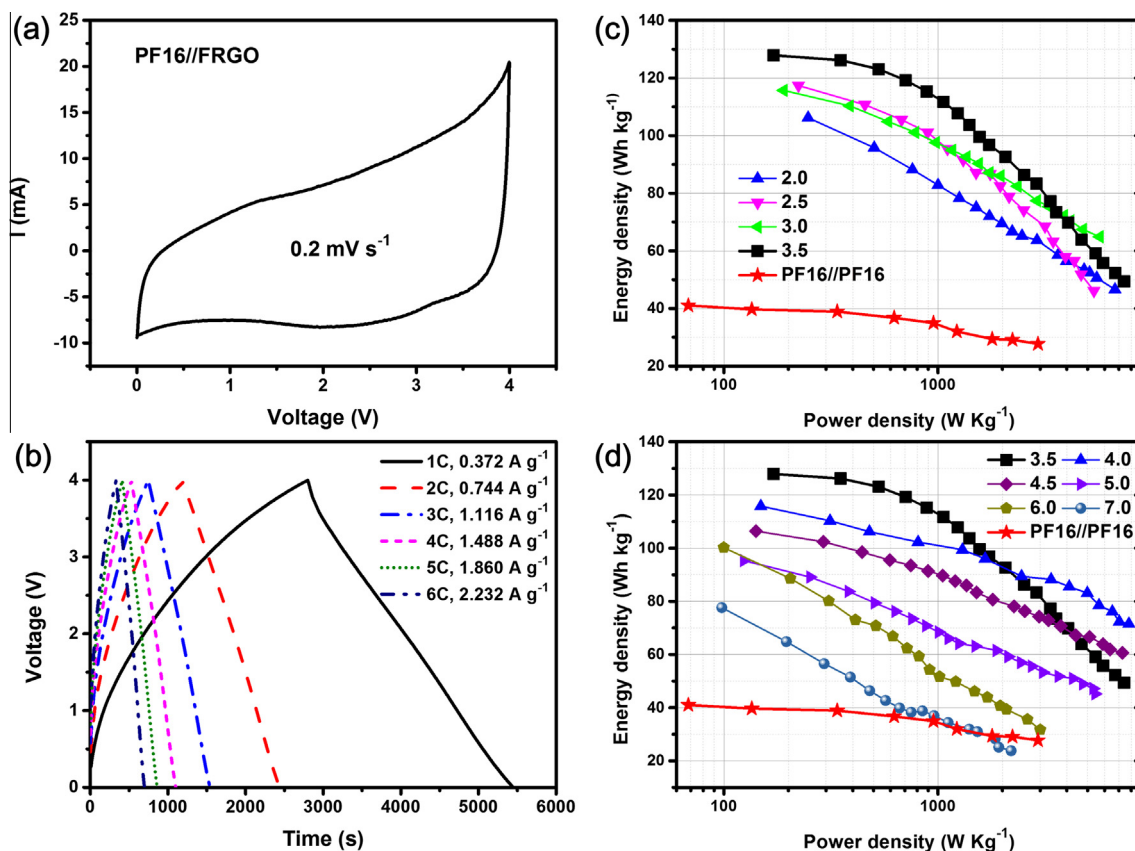


Fig. 5 – (a) CV curve of the LIC device PF16//FRGO with a mass ratio (m_+/m_-) of 3.5 at the scan rate of 0.2 mV s^{-1} . **(b)** Galvanostatic charge–discharge curves of LIC ($m_+/m_- = 3.5$) at different current densities of $0.372\text{--}2.232 \text{ A g}^{-1}$. **(c)** Ragone plots of LICs with different mass ratios (m_+/m_- of 2.0, 2.5, 3.0 and 3.5) and supercapacitor PF16//PF16. **(d)** Ragone plots of LICs with different mass ratios (m_+/m_- range from 3.5 to 7.0) and supercapacitor PF16//PF16. (A color version of this figure can be viewed online.)

complex, the actual electrochemical potential window of each electrode possibly may change compared with our designed potential window for each electrode, which should be more remarkable when the current density is high [27,53], and these changes would affect actual specific capacity exhibition of electrodes. More studies are needed for more and thorough understanding of this phenomenon.

The EIS results of the above mentioned devices are all shown in Fig. 6a. The enlarged Nyquist plot of symmetric supercapacitor (Fig. S16) shows PF16 has a high electrical conductivity and the intrinsic internal resistance is quite low ($\sim 0.36 \text{ Ohm}$). The small loop shows quite low interfacial charge transfer resistance at $\sim 3.7 \text{ Ohm}$, indicating a well-connected interface of PF16 and electrolyte ions. A short 45° Warburg region in the middle frequency region shows an excellent ion diffusion efficiency in the bulk of the electrode. The almost vertical line at low frequencies indicates an ideal capacitive performance of the device (as fast as 0.8 Hz , corresponding a fast recharging in 1.25 s) [17,54–57]. The plot of half-cell device PF16//Li has a large and obvious loop compared with PF16//PF16. Such a difference should be caused by the replacement of an EDLC type PF16 electrode with a Li metal foil electrode, and the latter electrode has a surficial metal electro deposition reaction which is slower than the formation of electric double layer electrochemically [58]. The plot

of FRGO//Li shows a compressed semicircle in the high-frequency region and an inclined line in the low-frequency region. The inclined line part is associated with impedance attributing to the diffusion of Li-ion through the graphene sheets. As a battery type material, the semicircle is small, indicating a quite small interfacial resistance of the FRGO [15,40]. The Nyquist plot of LIC PF16//FRGO demonstrates a small charge transfer impedance of both electrodes (its semicircle is only more obvious than the symmetric supercapacitor) and a superior ions diffusion process (compared with FRGO//Li) [58]. These results demonstrate the outstanding electrochemical properties of both electrode materials and their synergistic effect in LIC device. The LIC also exhibits a good cycle stability with the capacity retention of $\sim 80\%$ even after 3000 cycle numbers at a current density of 1.86 A g^{-1} (practical full discharge in 5–6 min), and the Coulombic efficiency always keeps at $\sim 100\%$ in such a long cycling process (Fig. 6b). Such a cycle stability is much better than most LIBs [8,12].

Based on the formula (2), the energy density of the device should increase with the increase of the operating voltage. Since PF16 still has a capacitive property in the potential window of $1.8\text{--}4.2 \text{ V vs Li/Li}^+$, higher energy density can be obtained by increasing the operating voltage of LIC. Fig. 7a shows the galvanostatic charge–discharge curves of LIC ($m_+/m_- = 3.5$) with different operating voltages. The curves

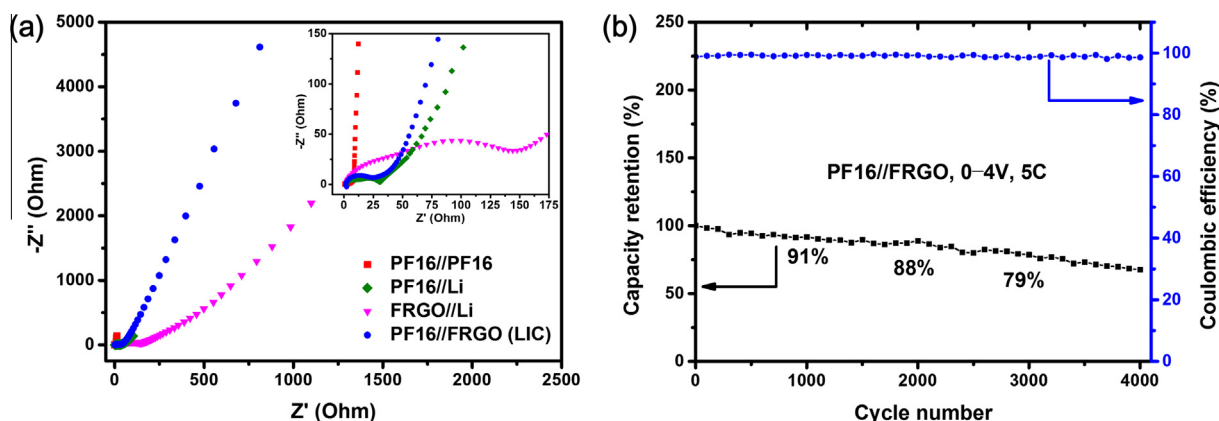


Fig. 6 – (a) Nyquist plots of devices of different structures: symmetric supercapacitor PF16//PF16, half-cells PF16//Li and FRGO//Li, LIC PF16//FRGO. The inset shows the expanded high-frequency region of the plots. (b) Cycle stability and Coulombic efficiency of LIC PF16//FRGO for more than 4000 cycles at a current density of 1.86 A g^{-1} (based on the mass of FRGO in the negative electrode). (A color version of this figure can be viewed online.)

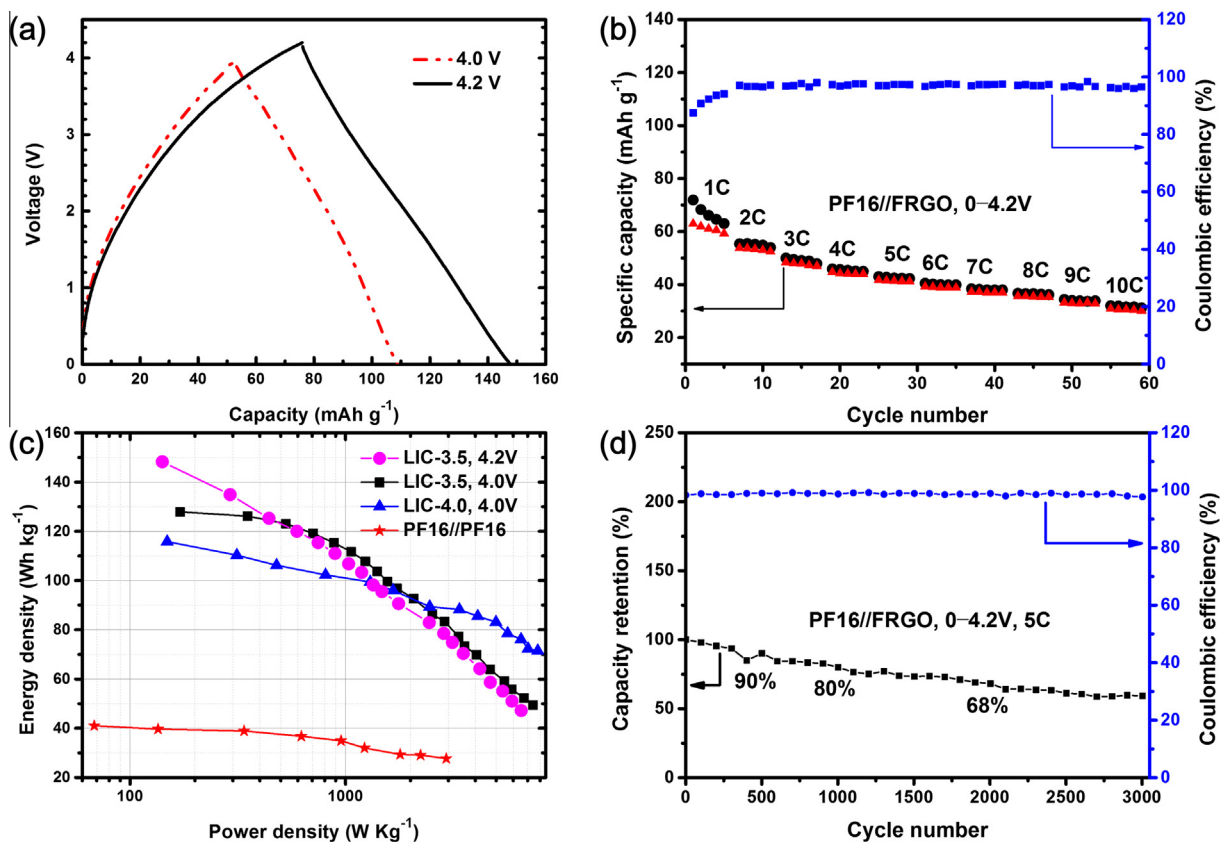


Fig. 7 – (a) Galvanostatic charge–discharge curves of an LIC ($m_+/m_- = 3.5$) in 0–4 V and 0–4.2 V at the current density of 0.372 A g^{-1} . (b) Rate performance and Coulombic efficiency of an LIC ($m_+/m_- = 3.5$) charged/discharged in 0–4.2 V. (c) The Ragone plot of the LIC ($m_+/m_- = 3.5$) charged/discharged in 0–4.2 V. (d) Cycle stability and Coulombic efficiency of an LIC ($m_+/m_- = 3.5$) charged/discharged in 0–4.2 V at a current density of 1.86 A g^{-1} . (A color version of this figure can be viewed online.)

of 4.2 V exhibit no distinct distortion compared with the curves of 4.0 V. The slightly low initial Coulombic efficiency (87.5%) at 1C and 4.2 V improves quickly in the following cycles (Fig. 7b). The Ragone plots (Fig. 7c) show the effect of operating voltage increase—LIC with the same mass ratio (3.5) could achieve an energy density as high as 148.3 Wh kg^{-1} with

almost no sacrifice of power density. Though this simple strategy for energy density enhancement could weaken the cycle stability (Fig. 7d), compared with the LIC operated in 0–4 V (Fig. 6b), it is still useful for some specific requirement.

As the active electrode materials are about 35–40% of the total mass of a packaged device [8,12], for our LIC no

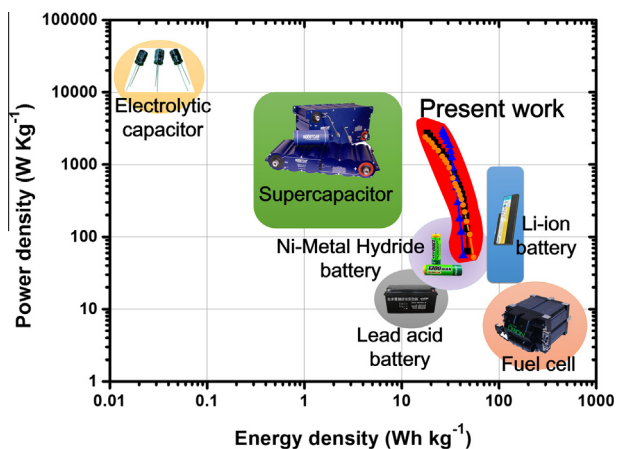


Fig. 8 – The Ragone plots of PF16//FRGO LIC compared with some commercial electronic energy storage devices (all based on total mass of packaged device). (A color version of this figure can be viewed online.)

conductive additive was used in both electrodes and PTFE as the binder only appeared in positive electrode, so we used 37% to calculate energy and power density of the packaged LIC. As shown in Fig. 8, the energy density of our packaged LIC could achieve 55 Wh kg^{-1} at the power density of 52 W kg^{-1} and still get close to 27 Wh kg^{-1} at the power density of 2886 W kg^{-1} . Therefore, the electrochemical performance of LIC indeed bridges LIB and EDLC in the Ragone plot. Besides, the pre-activated procedure of FRGO electrode can be improved to be more convenient and fast [58–61], which would make the PF16//FRGO LIC more practical.

4. Conclusion

In summary, starting from easily accessible GO and industrial carbon source, EDLC type material PF16 and battery type material FRGO are obtained by a simple hydrothermal–chemical activation method and a fast and green photoflash reduction method, respectively. Both PF16 and FRGO are investigated and their excellent electrochemical properties satisfy the requirements for assembling a superior LIC. And the results indicate that the designed LIC with PF16 as the positive electrode and FRGO as the negative electrode exhibited high energy densities of $148.3\text{--}71.5 \text{ Wh kg}^{-1}$ with the power densities from 141 to 7800 W kg^{-1} simultaneously. Furthermore, it is also accompanied with good cycle stability. Such a high performance of all-graphene based LIC is attributed to the usage of superior electrode materials which take the full advantage of graphene, and also the synergistic effect of both energy storage mechanisms of supercapacitor and LIB resulted from the LIC structure. The overall excellent performance indicates that our Li-ion capacitor may have great potential in applications such as consumer electronics and hybrid electric vehicles.

Acknowledgements

The authors gratefully acknowledge financial support from the MOST (Grants 2012CB933401 and 2014CB643502), NSFC

(Grants 21374050, 91433101, 51472124 and 51273093), MOE (B12015), PCSIRT (IRT1257) and NSF of Tianjin City (Grant 13RCGFGX01121).

Appendix A. Supplementary data

Supplementary data associated with this article can be found, in the online version, at <http://dx.doi.org/10.1016/j.carbon.2015.03.032>.

REFERENCES

- [1] Goodenough JB, Park KS. The Li-ion rechargeable battery: a perspective. *J Am Chem Soc* 2013;135(4):1167–76.
- [2] Nie M, Chalasani D, Abraham DP, Chen Y, Bose A, Lucht BL. Lithium ion battery graphite solid electrolyte interphase revealed by microscopy and spectroscopy. *J Phys Chem C* 2013;117(3):1257–67.
- [3] Liu J, Liu XW. Two-dimensional nanoarchitectures for lithium storage. *Adv Mater* 2012;24(30):4097–111.
- [4] Burke A. Ultracapacitor technologies and application in hybrid and electric vehicles. *Int J Energy Res* 2010;34(2):133–51.
- [5] Omar N, Daowd M, Hegazy O, Al Sakka M, Coosemans T, Van den Bossche P, et al. Assessment of lithium-ion capacitor for using in battery electric vehicle and hybrid electric vehicle applications. *Electrochim Acta* 2012;86:305–15.
- [6] Huang X, Yu H, Tan H, Zhu J, Zhang W, Wang C, et al. Carbon nanotube-encapsulated noble metal nanoparticle hybrid as a cathode material for li-oxygen batteries. *Adv Funct Mater* 2014;24(41):6516–23.
- [7] Li Y, Sheng K, Yuan W, Shi G. A high-performance flexible fibre-shaped electrochemical capacitor based on electrochemically reduced graphene oxide. *Chem Commun* 2013;49(3):291–3.
- [8] Stoller MD, Murali S, Quarles N, Zhu Y, Potts JR, Zhu X, et al. Activated graphene as a cathode material for Li-ion hybrid supercapacitors. *Phys Chem Chem Phys* 2012;14(10):3388–91.
- [9] El-Kady MF, Strong V, Dubin S, Kaner RB. Laser scribing of high-performance and flexible graphene-based electrochemical capacitors. *Science* 2012;335(6074):1326–30.
- [10] Liu C, Li F, Ma LP, Cheng HM. Advanced materials for energy storage. *Adv Mater* 2010;22(8):E28–62.
- [11] Simon P, Gogotsi Y. Materials for electrochemical capacitors. *Nat Mater* 2008;7(11):845–54.
- [12] Zhang F, Zhang T, Yang X, Zhang L, Leng K, Huang Y, et al. A high-performance supercapacitor-battery hybrid energy storage device based on graphene-enhanced electrode materials with ultrahigh energy density. *Energy Environ Sci* 2013;6(5):1623–32.
- [13] Huang Y, Liang J, Chen Y. An overview of the applications of graphene-based materials in supercapacitors. *Small* 2012;8(12):1805–34.
- [14] Leng K, Zhang F, Zhang L, Zhang T, Wu Y, Lu Y, et al. Graphene-based Li-ion hybrid supercapacitors with ultrahigh performance. *Nano Res* 2013;6(8):581–92.
- [15] Zhang F, Yang X, Xie Y, Yi N, Huang Y, Chen Y. Pyrolytic carbon-coated Si nanoparticles on elastic graphene framework as anode materials for high-performance lithium-ion batteries. *Carbon* 2015;82:161–7.
- [16] Han S, Wu D, Li S, Zhang F, Feng X. Graphene: a two-dimensional platform for lithium storage. *Small* 2013;9(8):1173–87.

- [17] Zhang L, Zhang F, Yang X, Long G, Wu Y, Zhang T, et al. Porous 3D graphene-based bulk materials with exceptional high surface area and excellent conductivity for supercapacitors. *Sci Rep* 2013;3:1408.
- [18] Wu J, Rui X, Wang C, Pei W-B, Lau R, Yan Q, et al. Nanostructured conjugated ladder polymers for stable and fast lithium storage anodes with high-capacity. *Adv Energy Mater* 2015. <http://dx.doi.org/10.1002/aenm.201402189>.
- [19] Cai R, Du Y, Zhang W, Tan H, Zeng T, Huang X, et al. Synthesis of porous amorphous FePO₄ nanotubes and their lithium storage properties. *Chem Eur J* 2013;19(5):1568–72.
- [20] Brownson DAC, Kampouris DK, Banks CE. An overview of graphene in energy production and storage applications. *J Power Sources* 2011;196(11):4873–85.
- [21] Yang X, Cheng C, Wang Y, Qiu L, Li D. Liquid-mediated dense integration of graphene materials for compact capacitive energy storage. *Science* 2013;341(6145):534–7.
- [22] Tao Y, Xie X, Lv W, Tang D-M, Kong D, Huang Z, et al. Towards ultrahigh volumetric capacitance: graphene derived highly dense but porous carbons for supercapacitors. *Sci Rep* 2013;3:2975.
- [23] Ghidui M, Lukatskaya MR, Zhao M-Q, Gogotsi Y, Barsoum MW. Conductive two-dimensional titanium carbide ‘clay’ with high volumetric capacitance. *Nature* 2014;516:78–81.
- [24] Zhang C, Lv W, Tao Y, Yang Q-H. Towards superior volumetric performance: design and preparation of novel carbon materials for energy storage. *Energy Environ Sci* 2015. <http://dx.doi.org/10.1039/C5EE00389J>.
- [25] Wang H, Yoshio M, Thapa AK, Nakamura H. From symmetric AC/AC to asymmetric AC/graphite, a progress in electrochemical capacitors. *J Power Sources* 2007;169(2):375–80.
- [26] Sivakkumar SR, Nerkar JY, Pandolfo AG. Rate capability of graphite materials as negative electrodes in lithium-ion capacitors. *Electrochim Acta* 2010;55(9):3330–5.
- [27] Cao WJ, Zheng JP. The effect of cathode and anode potentials on the cycling performance of Li-ion capacitors. *J Electrochem Soc* 2013;160(9):A1572–6.
- [28] Wang H, Yoshio M. Effect of cation on the performance of AC/graphite capacitor. *Electrochem Commun* 2008;10(3):382–6.
- [29] Cao WJ, Zheng JP. Li-ion capacitors using carbon-carbon electrodes. *ECS Trans* 2013;45(29):165–72.
- [30] Jain A, Aravindan V, Jayaraman S, Kumar PS, Balasubramanian R, Ramakrishna S, et al. Activated carbons derived from coconut shells as high energy density cathode material for Li-ion capacitors. *Sci Rep* 2013;3:3002.
- [31] Puthusseri D, Aravindan V, Madhavi S, Ogale S. Improving the energy density of Li-ion capacitors using polymer-derived porous carbons as cathode. *Electrochim Acta* 2014;130:766–70.
- [32] Y-g Wang, Y-y Xia. Hybrid aqueous energy storage cells using activated carbon and Lithium-intercalated compounds I. The C/LiMn₂O₄ system. *J Electrochem Soc* 2006;153(2):A450–4.
- [33] Chen L-M, Lai Q-Y, Hao Y-J, Huang J-h, Ji X-Y. Pseudo-capacitive properties of LiCoO₂/AC electrochemical capacitor in various aqueous electrolytes. *Ionics* 2008;14(5):441–7.
- [34] Dsoke S, Fuchs B, Gucciardi E, Wohlfahrt-Mehrens M. The importance of the electrode mass ratio in a Li-ion capacitor based on activated carbon and Li₄Ti₅O₁₂. *J Power Sources* 2015;282:385–93.
- [35] Ye L, Liang Q, Lei Y, Yu X, Han C, Shen W, et al. A high performance Li-ion capacitor constructed with Li₄Ti₅O₁₂/C hybrid and porous graphene macroform. *J Power Sources* 2015;282:174–8.
- [36] Naoi K, Simon P. New materials and new configurations for advanced electrochemical capacitors. *J Electrochem Soc* 2008;17(1):34–7.
- [37] Liu J. Charging graphene for energy. *Nat Nanotechnol* 2014;9(10):739–41.
- [38] Lahiri I, Choi W. Carbon nanostructures in Lithium ion batteries: past, present, and future. *Crit Rev Solid State* 2013;38(2):128–66.
- [39] Cao X, Shi Y, Shi W, Lu G, Huang X, Yan Q, et al. Preparation of novel 3D graphene networks for supercapacitor applications. *Small* 2011;7(22):3163–8.
- [40] Mukherjee R, Thomas AV, Krishnamurthy A, Koratkar N. Photothermally reduced graphene as high-power anodes for lithium-ion batteries. *ACS Nano* 2012;6(9):7867–78.
- [41] Bose S, Drzal LT. Role of thickness and intercalated water in the facile reduction of graphene oxide employing camera flash. *Nanotechnology* 2014;25(7):075702.
- [42] Gogotsi Y, Simon P. True performance metrics in electrochemical energy storage. *Science* 2011;334(6058):917–8.
- [43] Stoller MD, Ruoff RS. Best practice methods for determining an electrode material's performance for ultracapacitors. *Energy Environ Sci* 2010;3(9):1294–301.
- [44] Cote LJ, Cruz-Silva R, Huang J. Flash reduction and patterning of graphite oxide and its polymer composite. *J Am Chem Soc* 2009;131(31):11027–32.
- [45] Gao W, Singh N, Song L, Liu Z, Reddy ALM, Ci L, et al. Direct laser writing of micro-supercapacitors on hydrated graphite oxide films. *Nat Nanotechnol* 2011;6(8):496–500.
- [46] Li X, Hu Y, Liu J, Lushington A, Li R, Sun X. Structurally tailored graphene nanosheets as lithium ion battery anodes: an insight to yield exceptionally high lithium storage performance. *Nanoscale* 2013;5(24):12607–15.
- [47] Khantha M, Cordero N, Molina L, Alonso JA, Girifalco LA. Interaction of lithium with graphene: an ab initio study. *Phys Rev B* 2004;70(12):125422.
- [48] Yoo E, Kim J, Hosono E, Zhou H-s, Kudo T, Honma I. Large reversible Li storage of graphene nanosheet families for use in rechargeable lithium ion batteries. *Nano Lett* 2008;8(8):2277–82.
- [49] Dahn JR, Zheng T, Liu Y, Xue JS. Mechanisms for lithium insertion in carbonaceous materials. *Science* 1995;270(5236):590–3.
- [50] Wang G, Shen X, Yao J, Park J. Graphene nanosheets for enhanced lithium storage in lithium ion batteries. *Carbon* 2009;47(8):2049–53.
- [51] Wu Y-P, Wan C-R, Jiang C-Y, Fang S-B, Jiang Y-Y. Mechanism of lithium storage in low temperature carbon. *Carbon* 1999;37(12):1901–8.
- [52] Choi HS, Park CR. Theoretical guidelines to designing high performance energy storage device based on hybridization of lithium-ion battery and supercapacitor. *J Power Sources* 2014;259:1–14.
- [53] Li J, Gao F. Analysis of electrodes matching for asymmetric electrochemical capacitor. *J Power Sources* 2009;194(2):1184–93.
- [54] Lu Y, Zhang F, Zhang T, Leng K, Zhang L, Yang X, et al. Synthesis and supercapacitor performance studies of N-doped graphene materials using o-phenylenediamine as the double-N precursor. *Carbon* 2013;63:508–16.
- [55] Yang X, Zhang L, Zhang F, Zhang T, Huang Y, Chen Y. A high-performance all-solid-state supercapacitor with graphene-doped carbon material electrodes and a graphene oxide-doped ion gel electrolyte. *Carbon* 2014;72:381–6.
- [56] Choi BG, Yang M, Hong WH, Choi JW, Huh YS. 3D macroporous graphene frameworks for supercapacitors with high energy and power densities. *ACS Nano* 2012;6(5):4020–8.
- [57] Chen W-C, Wen T-C, Teng H. Polyaniline-deposited porous carbon electrode for supercapacitor. *Electrochim Acta* 2003;48(6):641–9.

-
- [58] Ren JJ, Su LW, Qin X, Yang M, Wei JP, Zhou Z, et al. Pre-lithiated graphene nanosheets as negative electrode materials for Li-ion capacitors with high power and energy density. *J Power Sources* 2014;264:108–13.
- [59] Forney MW, Ganter MJ, Staub JW, Ridgley RD, Landi BJ. Prelithiation of silicon–carbon nanotube anodes for lithium ion batteries by stabilized lithium metal powder (SLMP). *Nano Lett* 2013;13(9):4158–63.
- [60] Gourdin G, Smith PH, Jiang T, Tran TN, Qu D. Lithiation of amorphous carbon negative electrode for Li ion capacitor. *J Electroanal Chem* 2013;688:103–12.
- [61] Kim M, Xu F, Lee JH, Jung C, Hong SM, Zhang QM, et al. A fast and efficient pre-doping approach to high energy density lithium-ion hybrid capacitors. *J Mater Chem A* 2014;2(26):10029–33.